Editors' Suggestion

Magnetic structure and magnetoelectric effect in the centrosymmetric antiferromagnet $Cu_2(MoO_4)(SeO_3)$

Pharit Piyawongwatthana,[1,*] Kazuhiro Nawa,[1] Stuart Calder,[2] Daisuke Okuyama,[1] Hung-Cheng Wu,[1] and Taku J. Sato[1]

[1]*Institute of Multidisciplinary Research for Advanced Materials, Tohoku University, Sendai 980-8577, Japan*

[2]*Neutron Scattering Division, Oak Ridge National Laboratory, Oak Ridge, Tennessee 37831, USA*

(Received 30 November 2023; revised 23 March 2024; accepted 31 May 2024; published 17 June 2024)

Magnetic properties of $Cu_2(MoO_4)(SeO_3)$, an $S = \frac{1}{2}$ centrosymmetric antiferromagnet (AFM), were investigated using superconducting quantum interference device magnetometry, neutron diffraction, and magnetoelectric (ME) measurements. The magnetic susceptibility measurements indicate a broad peak at ∼50 K, followed by a phase transition into AFM order at $T_N = 23.6(1)$ K. Above T_N, a fit to the Curie-Weiss law gives a Curie-Weiss temperature $\Theta_{CW} = -68(1)$ K, suggesting the dominant AFM coupling. Neutron powder diffraction reveals that the Cu^{2+} spins are aligned AFM along the c axis with weak noncollinearity under the magnetic space group of $P2'_1/c$. The ME response indicates that a nondiagonal component of a ME tensor is active, supporting the simultaneous spatial and time reversal symmetry breaking under $P2'_1/c$.

DOI: 10.1103/PhysRevB.109.224420

I. INTRODUCTION

Low-dimensional quantum-spin systems have attracted continuous interest from physicists for many decades as hosts for many intriguing phenomena as well as playgrounds to test fundamental theory [1–3]. Exemplified by the one-dimensional (1D) antiferromagnetic (AFM) chains, such phenomena include the spin-Peierls transition in an alternating Heisenberg chain in $CuGeO_3$ [4,5], the Haldane gap formation in a Heisenberg chain with integer spins [6], the spin-singlet state in the alternating spin chain $(VO)_2E_2O_7$ [7], the multispinon excitations in $CuSO_4 \cdot 5D_2O$ [8], and the emergence of E_8 particles near the quantum critical point in the Ising chain AFM in the presence of a transverse magnetic field in $CoNb_2O_6$ and $BaCo_2V_2O_8$ [9,10] as well as multiple string excitations in an Ising chain AFM [11]. Having moderate interchain interactions, a system acquires two-dimensionality (2D) and starts to show very intriguing phenomena, such as the recent observation of bound spinon excitation in $Ca_3ReO_5Cl_2$ [12] and a dimensional crossover which arises from frustration in Cs_2CuCl_4 [13,14], to note a few. This way, discovery of low-dimensional quantum magnets with spin networks has been pivotal for finding quantum phenomena.

Recently, an $S = \frac{1}{2}$ AFM system $Cu_2(MoO_4)(SeO_3)$ has been discovered [15]. As depicted in Figs. 1(a) and 1(b), this compound crystallizes in a centrosymmetric monoclinic system with a space group of $P2_1/c$ and the following unit cell parameters: $\beta = 104.675(12)°$, $a = 8.148(5)$ Å, $b = 9.023(5)$ Å, and $c = 8.392(5)$ Å. The Cu^{2+} ions form an armchairlike chain along the crystallographic c axis, with each Cu^{2+} ion residing in a CuO_5 polyhedron carrying a spin $S = \frac{1}{2}$, which governs the magnetic properties of the system. Figure 1(c) illustrates the three different exchange interaction paths along the armchair chain: Cu1-O-Cu1, Cu1-O-Cu2, and Cu2-O-Cu2, with corresponding bond angles. These exchange paths are labeled as J_1, J_2, and J_3, with bond lengths of 2.990(1), 3.155(1), and 3.161(1) Å, respectively. Additionally, a longer superexchange pathway exists along the b axis where the CuO_5 chains are connected by SeO_3 and MoO_4 groups, involving Cu1-O-Se-O-Cu2 and Cu1-O-Mo-O-Cu2 bonds, with bond lengths of 4.555(3) and 4.794(3) Å, respectively. This leads to the presence of alternating magnetic interactions J_4 and J_5, as depicted in Fig. 1(d). Furthermore, due to the breaking of local inversion symmetry at the midpoint of the bond connecting Cu1-Cu2 atoms, active Dzyaloshinskii-Moriya (DM) interactions are expected to be present [17,18].

In the previous study, the magnetic susceptibility of a powder sample of $Cu_2(MoO_4)(SeO_3)$ was investigated, providing insights into the magnetic properties of this compound [15]. The results revealed that $Cu_2(MoO_4)(SeO_3)$ is a low-dimensional magnet, exhibiting an effective magnetic moment of $\mu_{eff} = 1.80$ μ_B, which is consistent with the theoretical value of 1.74 μ_B for Cu^{2+} ions. The Curie-Weiss temperature was estimated as −71.2(7) K, indicating the presence of AFM interactions in the system. These findings suggest that the primary exchange interaction occurs along the armchair chain in $Cu_2(MoO_4)(SeO_3)$.

To apprehend diverse physics of this plausibly low-dimensional quantum magnet, a detailed understanding of the magnetic properties, particularly the ordered magnetic structure, is essential. To date, however, there has been only limited research on the magnetic properties and magnetic structure of $Cu_2(MoO_4)(SeO_3)$, as described above. Therefore, the main objective of this paper is to investigate the magnetic properties and magnetic structure of this compound in detail. This paper is organized as follows: In Sec. II, we provide a comprehensive description of the sample preparations and experimental methods employed in this paper. In Sec. III, we present the results and discussion. Section III A focuses on the magnetic properties of $Cu_2(MoO_4)(SeO_3)$ obtained using

*Contact author: pharit@post.j-parc.jp

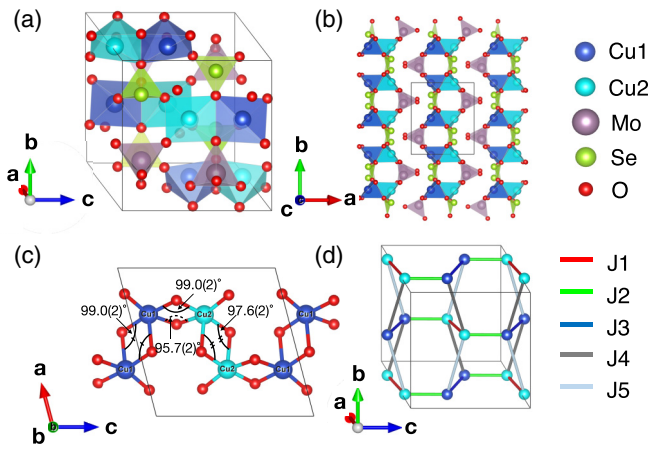

FIG. 1. Crystal structure and spin network of $Cu_2(MoO_4)(SeO_3)$. (a) and (b) The crystal structure of $Cu_2(MoO_4)(SeO_3)$ seen from two different directions. The Cu1 and Cu2 sites are distinguished by blue and cyan colors for clarity. The crystal structure consists of CuO_5 polyhedral, MoO_4 tetrahedra, and SeO_3 triangular plaquettes. The Cu^{2+} ions are connected via edge-sharing CuO_5 polyhedral, forming an armchairlike chain along the crystallographic c axis, while the large separation of atoms along the a axis suggests weaker interaction along this direction. (c) Details of the exchange paths in the armchairlike chain along the c axis. (d) Possible exchange paths in the armchairlike chain [J_1 (red), J_2 (green), J_3 (blue)], and paths bridging the chains [J_4 (gray), and J_5 (light gray)]. The crystal structures are visualized using VESTA software [16].

the single crystals. Magnetization measurements performed on the single-crystal samples reveal a magnetic phase transition occurring at $T_N \sim 23$ K and demonstrate spin anisotropy along the crystallographic c axis. In Sec. III B, we employ neutron powder diffraction and magnetic representation analysis to unveil the AFM order in $Cu_2(MoO_4)(SeO_3)$. An AFM order with $\mathbf{q} = (0, 0, 0)$ and the magnetic space group $P2_1'/c$ was concluded with most magnetic moments aligned parallel or antiparallel to the c axis. In Sec. III C, we present the results of magnetoelectric (ME) effect measurements. We found that $Cu_2(MoO_4)(SeO_3)$ becomes ME active upon AFM order, with the ME tensor being consistent with $P2_1'/c$. Finally, this paper concludes with a summary of the main findings in Sec. IV.

II. EXPERIMENTAL DETAILS

A powder sample of $Cu_2(MoO_4)(SeO_3)$ was synthesized through a hydrothermal reaction using high-purity CuO, MoO_3, and SeO_2 as starting materials [15]. The resulting powder sample of a pure phase of $Cu_2(MoO_4)(SeO_3)$ was used for neutron powder diffraction measurements. Additionally, this powder sample was utilized as the precursor for single-crystal growth using the chemical vapor transport technique, with NH_4Cl serving as the transport agent. In this process, a quartz ampule was filled with 500 mg of the $Cu_2(MoO_4)(SeO_3)$ powder and 0.4 mg/cm^3 NH_4Cl and evacuated. The ampule was then placed in a two-zone tube furnace, with the temperature of the source zone set at 510 °C and the deposition zone set at 460 °C. This temperature gradient was maintained for a duration of 2 wk, resulting in the growth of several single crystals with a maximum mass of ∼40 mg.

Magnetic susceptibility measurements were performed on a single crystal with the magnetic field applied along the a, b, and c crystallographic directions. A small single crystal with dimensions of $1 \times 1 \times 3$ mm^3 was precisely aligned using a four-circle x-ray diffractometer. The crystal was securely fixed to a plastic sheet using GE-7031 varnish and positioned on a sample stick during the measurements. The magnetic susceptibility was then measured as a function of temperature in the range between 2 and 300 K, using a superconducting quantum interference device (SQUID) magnetometer (MPMS-XL, Quantum Design) with an applied magnetic field of 10 kOe.

Neutron powder diffraction experiments were conducted at Oak Ridge National Laboratory (ORNL) using the HB-2A neutron powder diffractometer. Neutrons with a wavelength of $\lambda = 2.406$ Å were selected using a Ge 113 monochromator. The 6 g powder sample was packed into a cylindrical aluminum container with helium exchange gas and loaded in a closed-cycle refrigerator with the base temperature $T = 4$ K. Diffraction patterns were recorded over the 2θ range of 6 °–127 °. The structure refinement was carried out using the Rietveld method, utilizing the FULLPROF software suite [19]. Additionally, single-crystal neutron diffraction experiments were performed on coaligned single crystals weighing ∼280 mg. The measurements were carried out on the general-purpose triple-axis spectrometer (GPTAS) at JRR-3, Japan.

The ME measurement was conducted using a homemade ME measurement system combined with the commercial MPMS-XL SQUID magnetometer. To do this, we set the sample, sandwiched by two electrodes, in the middle of the gradiometer pickup coil of MPMS-XL and directly read the magnetic flux change induced by the electric field in the gradiometer as the current in the compensating coil coupled to the SQUID. The utilization of the SQUID to detect magnetization induced by electric fields was demonstrated by Kita *et al.* [20], and the commercial SQUID magnetometer was also used for this purpose in the past [21,22]. In our implementation, we applied an alternating electric field E_{ac} with an excitation frequency of $f = 35$ Hz and amplitude of 60 V, corresponding to the electric field amplitude 1.2 kV/cm. The time-domain signal from the SQUID readout was captured using a high-speed and high-resolution digital oscilloscope to capture the time-domain signal from the SQUID readout for a sufficiently long duration (typically 1.5 h at each temperature). Through numerical fast Fourier transform (FFT), we obtain the frequency domain spectrum over a wide frequency range and then use only the signal at specific frequencies of interest. This approach not only allows us to detect subtle ME signals down to 10^{-9} emu range with high precision by rejecting unrelated noise but also promptly identify the presence of higher harmonic components. Further details on the ME measurement will be provided in a separate publication.

III. RESULTS AND DISCUSSION

A. Magnetic properties

Figure 2 displays results of the magnetic susceptibility measurements with the applied field along the a, b, and c axes. The temperature dependence of the magnetic susceptibility

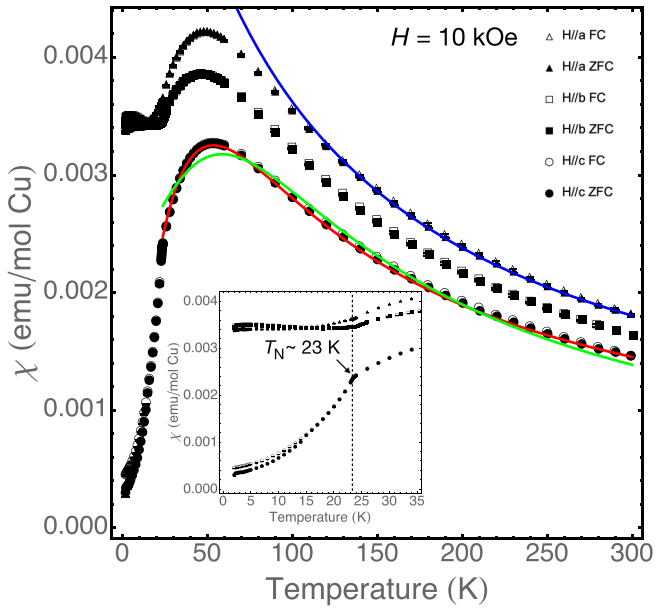

FIG. 2. Magnetic susceptibility measured on a single crystal of $Cu_2(MoO_4)(SeO_3)$ with an applied magnetic field of 10 kOe along the three crystallographic directions. The closed symbols represent the measurement in the zero-field-cooled (ZFC) runs, while the open symbols represent the measurement in the field-cooled (FC) runs. The blue curve represents the fitting results obtained using the Curie-Weiss law. The inset displays a magnification of the low-temperature magnetic susceptibility. The green and red curves are the fitting results of the Bonner-Fisher model and the alternating antiferromagnetic-antiferromagnetic (AFM-AFM) chain model, respectively. The dashed line around $T \sim 23$ K signifies the temperature corresponding to the AFM phase transition.

along three directions shows anisotropic behavior and reveals a broad maximum ∼50 K, indicating the development of short-range spin-exchange correlations. As shown in the inset of Fig. 2, a kink ∼23 K suggests the onset of a long-range magnetic ordering. A sharp drop in susceptibility is observed solely along the c axis, indicating AFM order with most spins aligning along this axis. Below T_N, the magnetic susceptibility remains nearly temperature independent for the a and b axes. A slight bifurcation between the zero-field cooling (ZFC) and field-cooling (FC) runs along the c axis can be observed below T_N. The Curie-Weiss temperature (Θ_{CW}) and the Curie constant (C) were extracted from the magnetic susceptibility data using the well-known Curie-Weiss law:

$$\chi(T) = \chi_0 + \frac{C}{T - \Theta_{CW}}.$$

Here, χ_0 represents the temperature-independent susceptibility, assumed to be the same along all three crystallographic axes, and Θ_{CW} is the Curie-Weiss temperature. The fitting was performed to the data in the temperature range of $140 < T < 300$ K. The Curie-Weiss fit curves are depicted by the green lines in Fig. 2. The Curie-Weiss and other fit parameters for each field direction are presented in Table I. The negative value of Θ_{CW} indicates dominant AFM exchange interactions in $Cu_2(MoO_4)(SeO_3)$. The effective magnetic moments μ_{eff} along the a and b axes, estimated from the

TABLE I. Fitted parameters of the magnetic susceptibility data for $H//a$, $H//b$, and $H//c$ axes using the Curie-Weiss law. The value of χ_0 was fixed at 0.00024(1) cm^3/mol Cu during the fitting process.

$H//$	Θ_{CW} (K)	C (cm^3 K/mol Cu)	μ_{eff} (μ_B)
a	−70(1)	0.578(2)	2.144(4)
b	−65(2)	0.510(2)	2.010(6)
c	−68(1)	0.443(2)	1.877(4)

Curie-Weiss constant, are significantly larger than the spin-only value, $\mu_{eff} = g\mu_B\sqrt{S(S+1)} = 1.73\ \mu_B$ for $g = 2$ and $S = \frac{1}{2}$. This discrepancy suggests the presence of spin-orbit coupling and orbital contributions to the magnetic moment, leading to the increase in μ_{eff}.

An attempt has been made to fit the $H//c$ data to 1D models, including a Bonner-Fisher AFM uniform-chain model [1,23], the alternating AFM-AFM chain model [24], and the alternating ferromagnetic (FM)-AFM chain model [25]. Satisfactory fits were obtained from both the Bonner-Fisher and the alternating AFM-AFM models, as depicted by the green and red lines in Fig. 2. The fitting was performed in the temperature range of $40 < T < 300$ K. We observed that the alternating AFM-AFM model provided a better fit to the lower temperature range. The obtained fitting parameters for the Bonner-Fisher model were $g = 2.07(1)$ and $J = 40.4(2)$ K, while for the alternating AFM-AFM chain model, they were $g = 2.06(1)$, $J_1 = 44.7(1)$ K, and $J_2 = 30.4(1)$ K. However, despite these satisfactory fits, both models are not consistent with the magnetic structure described in the subsequent section. In contrast, the alternating FM-AFM model, suggested by the magnetic structure, failed to reproduce the magnetic susceptibility data. This discrepancy between the models and the magnetic susceptibility data implies that this system is not 1D, and further nearest neighbors, such as J_4 and J_5, may play crucial roles in stabilizing the magnetic structure.

Figure 3 depicts magnetization measurements on the single-crystal $Cu_2(MoO_4)(SeO_3)$ as a function of the magnetic field, up to 5 T, along the three crystallographic axes. Above T_N ($T = 30$ K), the magnetization exhibits linear behavior within the measured field range. Below T_N ($T = 2$ K), the magnetization shows a similar linear response as observed in the 30 K data for $H//a$ and $H//b$. It is noteworthy that, when the magnetic field is applied along the c axis, the magnetization at 2 K approaches zero as the applied magnetic field tends to zero. Furthermore, the change in magnetization is significantly smaller than the data collected at 30 K. This behavior is attributed to the system entering an AFM state, where most spins align AFM along the c axis below T_N, which agrees with the observation from the magnetic susceptibility reduction below T_N. However, below T_N, starting from zero applied field, the magnetization slightly rises to a finite value with only a slight increase in magnetic field. A very weak FM is evident, as shown in the inset of Fig. 3. The origin of this weak FM remains unclear at this moment.

B. Neutron powder diffraction

To investigate the magnetic structure of the ordered phase, we conducted a powder neutron diffraction experiment.

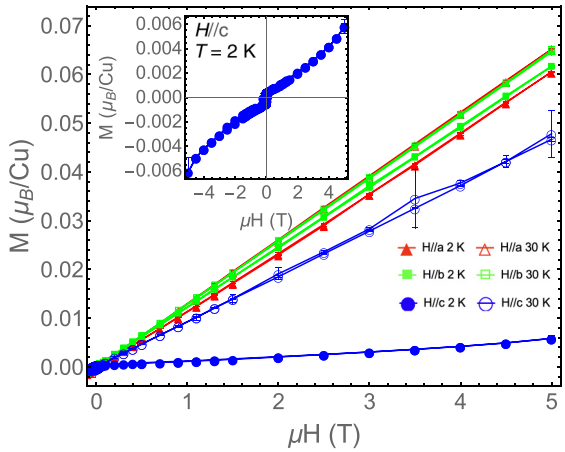

FIG. 3. Isothermal magnetization curves along the a, b, and c axes at 2 and 30 K. The magnetization along the c axis below T_N is close to zero suggesting that most of the spin in the antiferromagnetic (AFM) state is aligned AFM along the c axis. The inset shows a small step increase at zero magnetic field along the c axis in the magnetically ordered state.

Figure 4 presents the neutron powder diffraction data collected at 4 and 30 K at HB-2A. First, the crystal structure refinement was performed using the 30 K data. The data were refined against the space group $P2_1/c$ with the initial crystallographic parameters assumed as those reported in Ref. [15]. The 2θ regions between 61.5 ° and 63.5 °, 72.0 ° and 74.0 °, and >112 ° were excluded from the refinement to account for the influence of diffraction intensity arising from the aluminum can and refrigerator. The atomic displacement parameters U_{iso} were fixed to those in the earlier report, whereas the occupation number of each atom was fixed to one. The results of the Rietveld refinement were found to be consistent with the crystal structure of $Cu_2(MoO_4)(SeO_3)$ derived from a previous single-crystal x-ray diffraction study. The refined lattice parameters were $a = 8.104(4)$ Å, $b = 8.991(4)$ Å, $c = 8.386(4)$ Å, and $\beta = 104.745(1)°$. Detailed atomic coordinates are summarized in Table II.

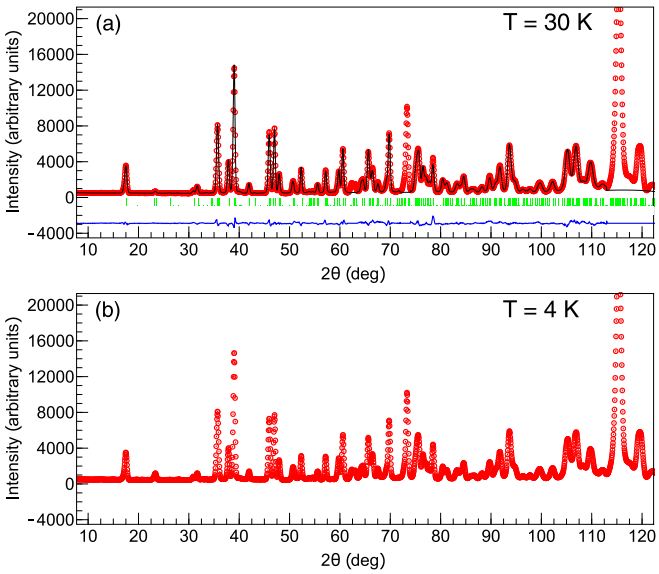

FIG. 4. (a) The neutron powder diffraction pattern recorded at 30 K. The observed data (red symbols) exhibit good agreement with the calculated pattern obtained from the Rietveld refinement (black line) assuming the monoclinic space group $P2_1/c$. The vertical green bars represent the nuclear reflections of $Cu_2(MoO_4)(SeO_3)$, while the blue line corresponds to the difference between the observed and calculated data. (b) The neutron powder diffraction pattern obtained at the base temperature ~4 K. A slight enhancement in the diffraction intensity was observed, superimposed on the nuclear reflections. The black arrows denote 110 reflection.

TABLE II. Crystallographic coordinates obtained from the Rietveld refinement performed on the neutron powder diffraction data using the space group $P2_1/c'$ at a temperature of $T = 30$ K. The refined unit cell parameters are $a = 8.104(4)$ Å, $b = 8.991(4)$ Å, $c = 8.386(4)$ Å, and $\beta = 104.745(1)°$. The atomic displacement parameters U_{iso} were fixed to those in the earlier report. The occupation number of each atom was fixed to one.

Atom	Wyckoff	x	y	z	U_{iso}
Cu1	4e	0.3169(5)	−0.0071(6)	0.3801(6)	0.0099
Cu2	4e	0.3166(6)	−0.0067(5)	0.02764(7)	0.0105
Mo	4e	0.1218(6)	0.2864(6)	0.162(1)	0.0074
Se	4e	0.3218(5)	−0.3271(4)	0.2029(8)	0.0072
O1	4e	0.3720(7)	−0.1442(6)	0.212(1)	0.0105
O2	4e	0.435(1)	−0.3869(6)	0.3887(8)	0.0109
O3	4e	0.438(1)	−0.3913(6)	0.078(1)	0.0106
O4	4e	0.2123(6)	0.1078(6)	0.1750(9)	0.0115
O5	4e	0.173(1)	0.3907(7)	0.0004(9)	0.0163
O6	4e	−0.0964(7)	0.2710(6)	0.108(2)	0.0187
O7	4e	0.1875(9)	0.3995(7)	0.341(1)	0.0188

No additional reflections were observed in the diffraction pattern below T_N. However, a small increase in intensity is observed on top of the nuclear Bragg reflection. This indicates a development of commensurate magnetic structure with the magnetic modulation vector $\mathbf{q} = (0, 0, 0)$. The strongest magnetic reflection is found around $2\theta \simeq 23.2°$, which corresponds to the 110 reflection. The 110 magnetic Bragg reflection was further investigated by scanning the reflection intensity as a function of temperature. Figure 5 shows the temperature dependence of the 110 reflection collected at GPTAS using coaligned single crystals. The temperature, at which integrated intensity starts to increase on cooling, coincides with the temperature $T \simeq 23$ K at which magnetic susceptibility shows the kink. The fit to the power law:

$$I(T) \propto \left(1 - \frac{T}{T_N}\right)^{2\beta},$$

gives $T_N = 23.6(1)$. The estimation of the critical exponent beta depends strongly on the fit range β in the vicinity of T_N ($23.2 < T < 23.55$ K) is ~0.4, which is rather close to the values for three-dimensional (3D) magnets (0.3689(3) for 3D-Heisenberg model [26], 0.3485(2) for 3D-XY model [27], and 0.3263(2) for 3D-Ising model [28]). This is nothing special since, in the vicinity of T_N, weak 3D interactions become relevant, and the system eventually behaves 3D. As shown in the inset of Fig. 5, the slope of the order parameter (in the logarithmic plot) becomes less steep on going away

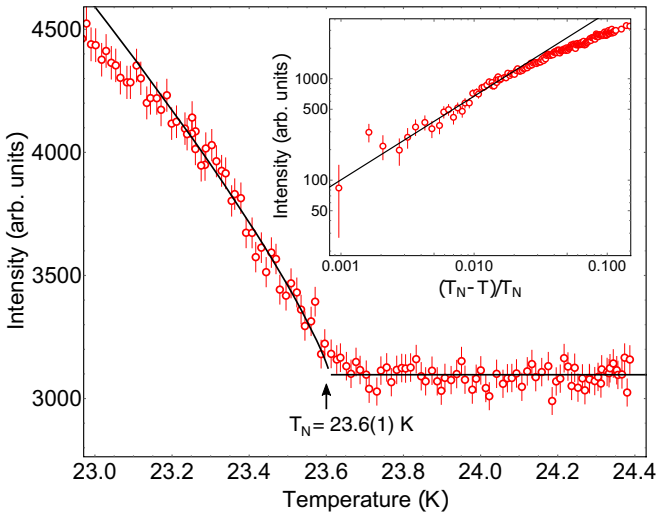

FIG. 5. The 110-reflection intensity as a function of temperature measured at the general-purpose triple-axis spectrometer (GPTAS). The black line denotes a power-law fit for the magnetic scattering intensity representing the order parameter. The inset shows the data and the fit in the logarithmic plot. Error bars represent 1 standard deviation.

from the critical point, indicating a smaller β exponent. This is indeed a sign of dominant low dimensionality of the present compound.

Next, we perform magnetic structure analysis of the ordered phase. For this purpose, candidates for initial magnetic structure models were obtained using the magnetic representation analysis [29]. The analysis based on the symmetry of the underlying crystal structure [30] was performed using the BasIreps software in the FULLPROF software package [19]. For $\mathbf{q} = (0, 0, 0)$ and the Wyckoff position $4e$ for the $P2_1/c$ space group, magnetic representations may be decomposed into four 1D irreducible representations (IRs) as:

$$\Gamma(4e) = 3\Gamma_1 + 3\Gamma_2 + 3\Gamma_3 + 3\Gamma_4.$$

The basis vectors (BVs) of each IR are summarized in Table III. We note that the IRs Γ_1, Γ_2, Γ_3, and Γ_4 correspond to the magnetic space groups $P2_1/c$, $P2_1/c'$, $P2'_1/c'$, and $P2'_1/c$, respectively. Assuming that there is only one order parameter for the magnetic phase transition in $Cu_2(MoO_4)(SeO_3)$, based on the Landau theory of second-order phase transition, the magnetic structure of the low-temperature phase should correspond to a single IR.

As discussed above with the magnetic susceptibility data, the AFM components of the Cu^{2+} moments predominantly align along the c axis. Among the four possible IRs, Γ_1 may reproduce the AFM order with the moments aligned along the c axis. However, it should be accompanied by the FM moment along the b axis, which is absent in the magnetization measurement. Hence, we can safely rule out Γ_1. Here, Γ_3 has a FM component within the ac plane; however, Γ_3 could not provide a satisfactory fit to the neutron diffraction data. In this paper, we, therefore, assume two initial magnetic structure models obtained as linear combinations of BVs of Γ_2 and Γ_4.

On performing the Rietveld analysis, we found that much weaker intensity of magnetic reflections than nuclear ones

TABLE III. Magnetic IRs and their BVs for the $4e$ site in the $P2_1/c$ space group with the magnetic modulation vector $\mathbf{q} = (0, 0, 0)$. The site index d is defined as follows: $d = 1$ corresponds to (x, y, z), $d = 2$ corresponds to $(-x + 1, y - \frac{1}{2}, -z + \frac{1}{2})$, $d = 3$ corresponds to $(-x + 1, -y + 1, -z + 1)$, and $d = 4$ corresponds to $(x, -y + \frac{3}{2}, z + \frac{1}{2})$. The x, y, and z correspond to atomic coordinates shown in Table II.

IRs	BV	$d = 1$	$d = 2$	$d = 3$	$d = 4$
Γ_1	ψ_1	1 0 0	−1 0 0	1 0 0	−1 0 0
	ψ_2	0 1 0	0 1 0	0 1 0	0 1 0
	ψ_3	0 0 1	0 0 −1	0 0 1	0 0 −1
Γ_2	ψ_1	1 0 0	−1 0 0	−1 0 0	1 0 0
	ψ_2	0 1 0	0 1 0	0 −1 0	0 −1 0
	ψ_3	0 0 1	0 0 −1	0 0 −1	0 0 1
Γ_3	ψ_1	1 0 0	1 0 0	1 0 0	1 0 0
	ψ_2	0 1 0	0 −1 0	0 1 0	0 −1 0
	ψ_3	0 0 1	0 0 1	0 0 1	0 0 1
Γ_4	ψ_1	1 0 0	1 0 0	−1 0 0	−1 0 0
	ψ_2	0 1 0	0 −1 0	0 −1 0	0 1 0
	ψ_3	0 0 1	0 0 1	0 0 −1	0 0 −1

hinder the simultaneous fitting of the nuclear and magnetic reflections in the diffraction pattern at $T = 4$ K. Hence, we first obtained the magnetic component by subtracting the 30 K data from the 4 K data and then performed Rietveld fitting to the subtracted magnetic component. The lattice parameters, atom fractional coordinates, occupation and isotropic atomic displacement parameter, and peak profile parameters were kept constant to those obtained from the fitting of the 30 K data. In addition, we impose a restriction that the size of the magnetic moments of Cu1 and Cu2 are equal. Figure 6 shows the magnetic contribution pattern observed at 4 K after the subtraction of the nuclear contribution seen at 30 K, together with the Rietveld refinement results assuming (a) Γ_2 and (b) Γ_4 IRs. The refinement result for Γ_2 shows that the magnetic moments are aligned almost along the b axis below the transition temperature. On the other hand, the refinement result on Γ_4 shows that the magnetic moments are aligned almost along the c axis. Since the latter is consistent with the magnetic anisotropy below T_N, Γ_4 is more likely the magnetic structure of $Cu_2(MoO_4)(SeO_3)$ in the magnetically ordered state. The magnetic R factors from the refinement for Γ_2 and Γ_4 yield 11.70 and 9.48%, respectively, with the better agreement achieved by Γ_4. The obtained magnetic moments are $\mathbf{m}_{Cu1} = [-0.44(5), 0.18(7), 0.69(5)]$ μ_B and $\mathbf{m}_{Cu2} = [0.06(6), 0.00(8), 0.73(3)]$ μ_B for Γ_4, defined in the lattice coordinate system. The ordered moment size is 0.73(6) μ_B for both Cu1 and Cu2 ions. This value of the ordered moment, which is consistent with the value obtained from powder neutron diffraction, is slightly lower than the expected value of 1 μ_B. The discrepancy could be a result from the quantum fluctuations that play a role in reducing the ordered moment. The resulting magnetic structure is illustrated in Fig. 7 for both Γ_2 and Γ_4 models. The noncollinearity of Cu1 and Cu2 spins away from the c axis supports the idea that unusual alternating DM interactions on the bond connecting Cu1 and Cu2 atoms are active in this compound. Another possible factor is the competition between the exchange

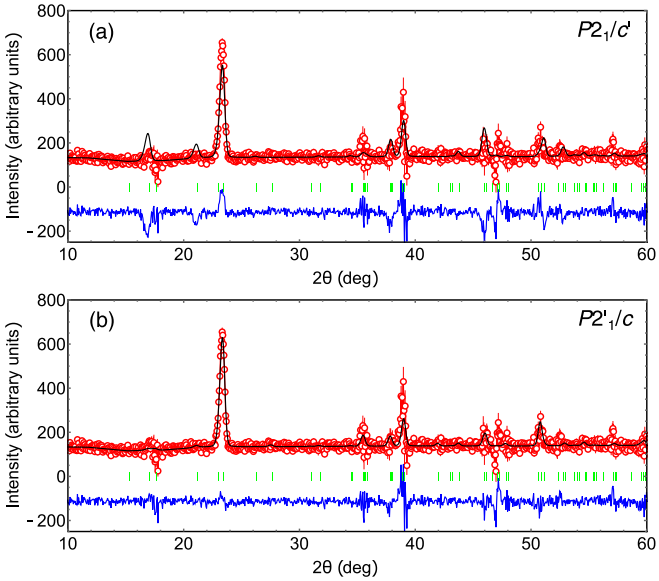

FIG. 6. The difference in data between 4 and 30 K reveals the presence of magnetic Bragg scattering. The magnetic-structure refinements based on the irreducible representations (a) Γ_2 and (b) Γ_4, are shown by the black lines. They are corresponding to the magnetic space groups $P2_1/c'$ and $P2'_1/c$, respectively. The vertical green lines indicate the positions of the magnetic Bragg peaks, with 110 being the strongest peak. The blue line represents the difference between the observed and calculated patterns. Error bars correspond to 1 standard deviation.

interactions within the chain. It is anticipated that J_1 and J_3 are AFM, while J_2 is FM. It would be interesting to investigate this effect of the local DM interaction in spin dynamics of this system in future.

C. ME effect

In the above, we have postulated one magnetic structure from the neutron magnetic diffraction data. Nonetheless, the limited statistics due to the small Cu moment size inevitably results in the large uncertainty in the diffraction data and consequently in the postulated magnetic structure model. Hence, it is certainly worthwhile to confirm the magnetic structure by another technique. It is known that the linear

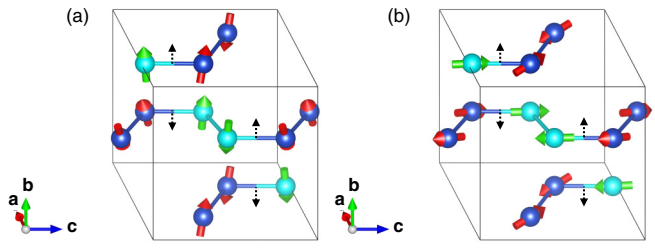

FIG. 7. The magnetic structure of $Cu_2(MoO_4)(SeO_3)$ is depicted for (a) Γ_2 ($P2_1/c'$) and (b) Γ_4 ($P2'_1/c$) irreducible representations. The magnetic moments at the Cu1 and Cu2 sites are represented by red and green arrows, respectively. The black arrows indicate the components of the Dzyaloshinskii-Moriya (DM) interactions along the *b* axis.

TABLE IV. Linear ME tensor for the Γ_2 IR corresponding to the magnetic space group $P2_1/c'$.

α_{ij}		j	
i	α_{11}	–	α_{13}
	–	α_{22}	–
	α_{31}	–	α_{33}

ME effect is highly sensitive to the magnetic symmetry of the system [31–33]. Among the four magnetic space groups $P2_1/c$, $P2_1/c'$, $P2'_1/c'$, and $P2'_1/c$ derived in the magnetic representation analysis, $P2_1/c$ and $P2'_1/c'$ do not allow the linear ME effect since they do not break inversion symmetry. On the other hand, $P2_1/c'$ and $P2'_1/c$ allow the linear ME effect; their ME tensors are listed in Tables IV and V, respectively. The active components differ between the two magnetic space groups; while diagonal components are active for $P2_1/c'$, off-diagonal components are active for $P2'_1/c$. Hence, by measuring specific ME tensor components using the single-crystalline sample, we may obtain a clear distinction between the four magnetic space groups assumed for the AFM phase in $Cu_2(MoO_4)(SeO_3)$.

The ME coefficient α was measured for the two electric (E) and magnetic field (H) settings: $H//c$, $E//b$ (α_{32}) and $H//b$, $E//b$ (α_{22}). At each temperature, the induced magnetization was measured as a function of time under E_{ac} with the frequency $f = 35$ Hz. Then the FFT was performed to obtain the frequency spectrum of magnetization fluctuation. Shown in Figs. 8(a) and 8(c) are representative spectra of magnetization fluctuation around the ac frequency 35 Hz. The induced magnetization fluctuation can be clearly seen for the $H//c$, $E//b$ setting, whereas it is absent for $H//b$, $E//b$. The corresponding temperature dependence of the integrated intensity of the 35 Hz peak is plotted in Figs. 8(b) and 8(d). We observed a significant increase in the α_{32} coefficient ~23 K, which coincides with the onset of the magnetic phase transition. This coincidence indicates a clear connection between the ME effect and the magnetic phase transition in this compound. The temperature dependence of α_{32} shows a peak in magnitude just below T_N and decreases with temperature. This observation could be understood in terms of the response of spin fluctuation near the phase transition temperature, where spin fluctuation is significant [34]. A similar observation is also noted in other multiferroic systems such as Cr_2O_3, $MnTiO_3$, and Fe_2TeO_6 [35–38]. On the other hand, no noticeable change was detected for the diagonal component α_{22} in the vicinity of T_N. This result indicates that the magnetic point symmetry of the AFM phase is $2'_1/c$, being consistent with the neutron diffraction conclusion. We did not observe the higher harmonic $2f$

TABLE V. Linear ME tensor for the Γ_4 IR corresponding to the magnetic space group $P2'_1/c$.

α_{ij}		j	
i	–	α_{12}	–
	α_{21}	–	α_{23}
	–	α_{32}	–

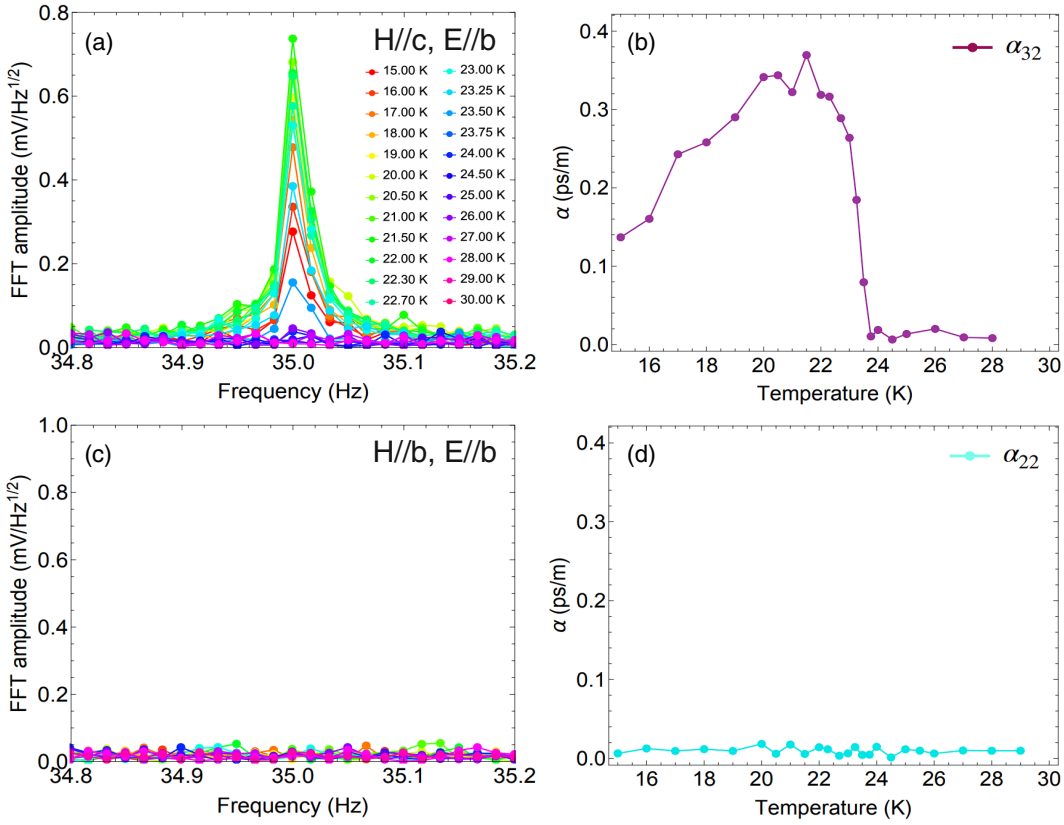

FIG. 8. (a) and (c) show the temperature dependence of the amplitude of the Fourier spectrum of $Cu_2(MoO_4)(SeO_3)$ under two experimental configurations: *H*//*c*, *E*//*b* and *H*//*b*, *E*//*b*, respectively. (b) and (d) present the corresponding magnetoelectric coefficients α_{32} and α_{22} as a function of temperature.

component, confirming linear ME effect. We, hence, conclude that $Cu_2(MoO_4)(SeO_3)$ is a rare example of low-dimensional quantum magnet activating the linear ME effect due to the simultaneous breaking of spatial and time-reversal symmetry by the AFM order. It should be noted that a similar ME effect was reported in the low-dimensional quantum magnet with the magnetic space group $P2_1'/c$ in Refs. [39,40]. We also note here that the ME coefficient observed in $Cu_2(MoO_4)(SeO_3)$ is relatively small compared with other typical linear ME compounds such as Cr_2O_3 [35,36], $MnTiO_3$ [37], Co_3O_4 [41], and $NdCrTiO_5$ [42].

IV. CONCLUSIONS

The magnetic properties and magnetic structure of $Cu_2(MoO_4)(SeO_3)$ were investigated using SQUID magnetometry and neutron powder diffraction techniques. The results indicate that $Cu_2(MoO_4)(SeO_3)$ exhibits AFM order at the transition temperature $T_N = 23.6(1)$ K. Below T_N, the magnetic order in $Cu_2(MoO_4)(SeO_3)$ is commensurate with the chemical unit cell, characterized by the ordering wave vector $\mathbf{q} = (0, 0, 0)$, and exhibits a magnetic moment of 0.73(6 μ_B per Cu^{2+} ion). The magnetic structure can be described by the magnetic space group $P2_1'/c$; the magnetic moments dominantly align along the *c* axis, with weak noncollinearity due to the local alternating DM interaction. The magnetization measurement under E_{ac} indicates a clear appearance of the linear ME effect in the AFM phase, being consistent with the $P2_1'/c$ magnetic space group. We hence conclude that $Cu_2(MoO_4)(SeO_3)$ is an interesting example of quantum magnets activating the ME effect due to the simultaneous breaking of spatial and time-reversal symmetry by the AFM order.

ACKNOWLEDGMENTS

The authors thank S. Kimura and K. Ohgushi for stimulating discussion. This paper was partly supported by Grants-In-Aid for Scientific Research (Grants No. 23KK0051, No. 23K03296, No. 22H00101, No. 20K14395, No. 19KK0069, and No. 19H05824) from MEXT, Japan. A portion of this research used resources at the High Flux Isotope Reactor, a Department of Energy (DOE) Office of Science User Facility operated by the ORNL, and was partly supported by the U.S.-Japan Collaborative Program on Neutron Scattering. The work at JRR-3 was partly supported by the general user program of the Institute for Solid State Physics, University of Tokyo (Proposal No. 21501). The work at IMRAM was partly supported by the "Crossover Alliance to Create the Future with People, Intelligence and Materials" from MEXT, Japan.

[1] J. C. Bonner and M. E. Fisher, Linear magnetic chains with anisotropic coupling, Phys. Rev. **135**, A640 (1964).

[2] S. Sachdev, Quantum magnetism and criticality, Nat. Phys. **4**, 173 (2008).

[3] A. Vasiliev, O. Volkova, E. Zvereva, and M. Markina, Milestones of low-D quantum magnetism, npj Quantum Mater. **3**, 18 (2018).

[4] M. Hase, I. Terasaki, and K. Uchinokura, Observation of the spin-Peierls transition in linear Cu^{2+} (spin-$\frac{1}{2}$) chains in an inorganic compound $CuGeO_3$, Phys. Rev. Lett. **70**, 3651 (1993).

[5] J. Riera and A. Dobry, Magnetic susceptibility in the spin-Peierls system $CuGeO_3$, Phys. Rev. B **51**, 16098 (1995).

[6] F. D. M. Haldane, Nonlinear field theory of large-spin Heisenberg antiferromagnets: Semiclassically quantized solitons of the one-dimensional easy-axis Néel state, Phys. Rev. Lett. **50**, 1153 (1983).

[7] A. W. Garrett, S. E. Nagler, D. A. Tennant, B. C. Sales, and T. Barnes, Magnetic excitations in the $S = \frac{1}{2}$ alternating chain compound $(VO)_2E_2O_7$, Phys. Rev. Lett. **79**, 745 (1997).

[8] M. Mourigal, M. Enderle, A. Klöpperpieper, J.-S. Caux, A. Stunault, and H. M. Rønnow, Fractional spinon excitations in the quantum Heisenberg antiferromagnetic chain, Nat. Phys. **9**, 435 (2013).

[9] R. Coldea, D. A. Tennant, E. M. Wheeler, E. Wawrzynska, D. Prabhakaran, M. Telling, K. Habicht, P. Smeibidl, and K. Kiefer, Quantum criticality in an Ising chain: Experimental evidence for emergent E_8 symmetry, Science **327**, 177 (2010).

[10] Z. Zhang, K. Amelin, X. Wang, H. Zou, J. Yang, U. Nagel, T. Rõõm, T. Dey, A. A. Nugroho, T. Lorenz *et al.*, Observation of E_8 particles in an Ising chain antiferromagnet, Phys. Rev. B **101**, 220411(R) (2020).

[11] Z. Wang, J. Wu, W. Yang, A. K. Bera, D. Kamenskyi, A. T. M. N. Islam, S. Xu, J. M. Law, B. Lake, C. Wu *et al.*, Experimental observation of Bethe strings, Nature (London) **554**, 219 (2018).

[12] K. Nawa, D. Hirai, M. Kofu, K. Nakajima, R. Murasaki, S. Kogane, M. Kimata, H. Nojiri, Z. Hiroi, and T. J. Sato, Bound spinon excitations in the spin-$\frac{1}{2}$ anisotropic triangular antiferromagnet $Ca_3ReO_5Cl_2$, Phys. Rev. Res. **2**, 043121 (2020).

[13] R. Coldea, D. A. Tennant, A. M. Tsvelik, and Z. Tylczynski, Experimental realization of a 2D fractional quantum spin liquid, Phys. Rev. Lett. **86**, 1335 (2001).

[14] R. Coldea, D. A. Tennant, and Z. Tylczynski, Extended scattering continua characteristic of spin fractionalization in the two-dimensional frustrated quantum magnet Cs_2CuCl_4 observed by neutron scattering, Phys. Rev. B **68**, 134424 (2003).

[15] S. Y. Zhang, H. L. Jiang, C. F. Sun, and J. G. Mao, Syntheses, crystal structures, and properties of five new transition metal molybdenum(VI) selenites and tellurites, Inorg. Chem. **48**, 11809 (2009).

[16] K. Momma and F. Izumi, VESTA: A three-dimensional visualization system for electronic and structural analysis, J. Appl. Cryst. **41**, 653 (2008).

[17] I. Dzyaloshinsky, A thermodynamic theory of "weak" ferromagnetism of antiferromagnetics, J. Phys. Chem. Solids. **4**, 241 (1958).

[18] T. Moriya, Anisotropic superexchange interaction and weak ferromagnetism, Phys. Rev. **120**, 91 (1960).

[19] J. Rodríguez-Carvajal, Recent advances in magnetic structure determination by neutron powder diffraction, Phys. B: Condens. **192**, 55 (1993).

[20] E. Kita, A. Tasaki, and K. Siratori, Application of SQUID magnetometer to the measurement of magnetoelectric effect in Cr_2O_3, Jpn. J. Appl. Phys. **18**, 1361 (1979).

[21] E. Kita, DC magnetoelectric effect measurements by a squid magnetometer, Ferroelectrics **162**, 397 (1994).

[22] P. Borisov, A. Hochstrat, V. V. Shvartsman, and W. Kleemann, Superconducting quantum interference device setup for magnetoelectric measurements, Rev. Sci. Instrum. **78**, 106105 (2007).

[23] W. E. Estes, D. P. Gavel, W. E. Hatfield, and D. J. Hodgson, Magnetic and structural characterization of dibromo- and dichlorobis(thiazole)copper(II), Inorg. Chem. **17**, 1415 (1978).

[24] J. W. Hall, W. E. Marsh, R. R. Weller, and W. E. Hatfield, Exchange coupling in the alternating-chain compounds catena-Di-μ-chloro-bis(4-methylpyridine)copper(II), catena-Di-μ-bromobis(N-methylimidazole)copper(II), catena-[hexanedione bis(thiosemicarbazonato)]copper(II), and catena-[octanedione bis (thiosemicarbazonato)]copper(II), Inorg. Chem. **20**, 1033 (1981).

[25] J. J. Borras-Almenar, E. Coronado, J. Curely, R. Georges, and J. C. Gianduzzo, Alternating chains with ferromagnetic and antiferromagnetic interactions. Theory and magnetic properties, Inorg. Chem. **33**, 5171 (1994).

[26] M. Campostrini, M. Hasenbusch, A. Pelissetto, P. Rossi, and E. Vicari, Critical exponents and equation of state of the three-dimensional Heisenberg universality class, Phys. Rev. B **65**, 144520 (2002).

[27] M. Campostrini, M. Hasenbusch, A. Pelissetto, P. Rossi, and E. Vicari, Critical behavior of the three-dimensional XY universality class, Phys. Rev. B **63**, 214503 (2001).

[28] A. M. Ferrenberg, J. Xu, and D. P. Landau, Pushing the limits of Monte Carlo simulations for the three-dimensional Ising model, Phys. Rev. E **97**, 043301 (2018).

[29] Y. Izyumov and V. Naish, Symmetry analysis in neutron diffraction studies of magnetic structures: 1. A phase transition concept to describe magnetic structures in crystals, J. Magn. Magn. Mater. **12**, 239 (1979).

[30] E. F. Bertaut, Representation analysis of magnetic structures, Acta Cryst. A **24**, 217 (1968).

[31] S. Picozzi, K. Yamauchi, B. Sanyal, I. A. Sergienko, and E. Dagotto, Dual nature of improper ferroelectricity in a magnetoelectric multiferroic, Phys. Rev. Lett. **99**, 227201 (2007).

[32] Y. J. Choi, H. T. Yi, S. Lee, Q. Huang, V. Kiryukhin, and S.-W. Cheong, Ferroelectricity in an Ising chain magnet, Phys. Rev. Lett. **100**, 047601 (2008).

[33] T. Arima, Spin-driven ferroelectricity and magneto-electric effects in frustrated magnetic systems, J. Phys. Soc. Japan **80**, 052001 (2011).

[34] M. Mostovoy, A. Scaramucci, N. A. Spaldin, and K. T. Delaney, Temperature-dependent magnetoelectric effect from first principles, Phys. Rev. Lett. **105**, 087202 (2010).

[35] M. Fiebig, Revival of the magnetoelectric effect, J. Phys. D: Appl. Phys. **38**, R123 (2005).

[36] A. Iyama and T. Kimura, Magnetoelectric hysteresis loops in Cr_2O_3 at room temperature, Phys. Rev. B **87**, 180408(R) (2013).

[37] T. Sato, N. Abe, S. Kimura, Y. Tokunaga, and T. Arima, Magnetochiral dichroism in a collinear antiferromagnet with no magnetization, Phys. Rev. Lett. **124**, 217402 (2020).

[38] S. Buksphan, E. Fischer, and R. M. Hornreich, Magnetoelectric and Mössbauer studies of Fe_2TeO_6, Solid State Commun. **10**, 657 (1972).

[39] S. Jodlauk, P. Becker, J. A. Mydosh, D. I. Khomskii, T. Lorenz, S. V. Streltsov, D. C. Hezel, and L. Bohaty, Pyroxenes: A new class of multiferroics, J. Phys.: Condens. Matter **19**, 432201 (2007).

[40] G. Nénert, M. Isobe, I. Kim, C. Ritter, C. V. Colin, A. N. Vasiliev, K. H. Kim, and Y. Ueda, Interplay between low dimensionality and magnetic frustration in the magnetoelectric pyroxenes $LiCrX_2O_6$ (X = Ge, Si), Phys. Rev. B **82**, 024429 (2010).

[41] R. Saha, S. Ghara, E. Suard, D. H. Jang, K. H. Kim, N. V. Ter-Oganessian, and A. Sundaresan, Magnetoelectric effect in simple collinear antiferromagnetic spinels, Phys. Rev. B **94**, 014428 (2016).

[42] J. Hwang, E. S. Choi, H. D. Zhou, J. Lu, and P. Schlottmann, Magnetoelectric effect in $NdCrTiO_5$, Phys. Rev. B **85**, 024415 (2012).